Three-Dimensional Scattering and Inverse Scattering From a Disturbed Region in Planarly Layered Cold Unmagnetized Plasma Media

Paiju Wen, Yongjin Chen, Feng Han, Na Liu, Hai Liu, *Member, IEEE*, and Qing Huo Liu, *Fellow, IEEE*

Abstract—We apply the forward scattering and inverse scattering algorithms to a cold unmagnetized plasma region within a multilayered background medium. Each layer has a different plasma frequency. The disturbed region in the plasma has an arbitrary shape, so it is an electromagnetic wave scatterer and can exist in any layer. The stabilized biconjugate-gradient fast Fourier transform (BCGS-FFT) algorithm is used to compute the scattered field. The scattered fields calculated by the BCGS-FFT yield excellent agreement with simulated results from the commercial software. In the inverse scattering process, the variational Born iterative method is used to reconstruct the relative permittivity, and thus the plasma frequency of the disturbed region. Multiple frequencies are adopted to determine the dispersive property of the plasma medium.

Index Terms—Biconjugate-gradient fast Fourier transform (BCGS-FFT) method, cold unmagnetized plasma, disturbed region in plasma, variational born iterative method (VBIM).

I. INTRODUCTION

ELECTROMAGNETIC (EM) wave scattering and inverse scattering are important topics in EMs. Their applications are valuable for military and geologic sensing [1], [2] such as landmine detection and subsurface anomaly imaging with ground penetrating radar. However, in view of the complex environments of the underground, the detection background is just assumed to be regular nonplasma medium in the research to date.

In this letter, the multilayered cold unmagnetized plasma media is considered as the background. The cold plasma, which is common in the ionosphere of the earth [3], has dispersive properties. A disturbed region, also made of a cold unmagnetized plasma [4], acts as the scatterer. There are numerous forward scattering algorithms, such as the conjugate gradient fast Fourier transform (CG-FFT) method, bi-CG FFT (BCG-FFT) method [5], multilevel fast-multipole method [6], and adaptive integral method [7] that have been applied to the forward scattering. In this letter, we adopt the stabilized

BCG-FFT (BCGS-FFT) algorithm [8], [9] as the forward solver to compute the scattered field. This algorithm can be applied to several 3-D applications including induction well logging problems [10]. Besides, it has been successfully used to solve EM scattering problems in layered media [11].

Up till now, several algorithms on the inverse scattering problems have been proposed, such as the distorted Born iterative method [12] and contrast source inversion [13]. The genetic algorithm, which was previously popular for seismic data processing, is later introduced to EM inversion of 3-D buried objects [14]. In addition, Zhong and Chen [15] proposed the multiple signal classification method to determine the locations of multiple-scattering small anisotropic spheres. Other inversion methods such as the subspace-based optimization method are also applied to the reconstruction of the buried scatters [16]. In this letter, we apply the variational Born iterative method (VBIM) to reconstruct the electrical properties of the disturbed region in layered plasma media. The VBIM is first introduced in [17] for conductivity reconstruction in an axisymmetric medium for the induction well logging application. In [18], it is successfully used to simultaneously reconstruct the permittivity and permeability of the 3-D objects. In our work, taking advantage of the scattered field computed by the BCGS-FFT, we apply the VBIM to reconstruct the electrical parameters of the disturbed region in layered cold unmagnetized plasma media.

II. THEORY

The dispersive property of the cold unmagnetized plasma can be expressed by the Drude model

$$\varepsilon_r = 1 - \frac{\omega_p^2}{\omega^2} \tag{1}$$

where ε_r denotes the relative permittivity, ω_p is the plasma frequency, and ω is angular frequency of the EM wave. The plasma frequency is approximately proportional to the square root of electron density, and is defined as

$$\omega_p = \sqrt{\frac{n_e e^2}{m_e \varepsilon_0}} \approx 56.4\sqrt{n_e} \tag{2}$$

where n_e is the electron density, m_e is the mass of one single electron, and e is the electron charge. According to the theory of the EM wave propagation, EM waves can propagate through the cold unmagnetized plasma medium only if ω is larger than ω_p. The plasma frequency ω_p is a fundamental
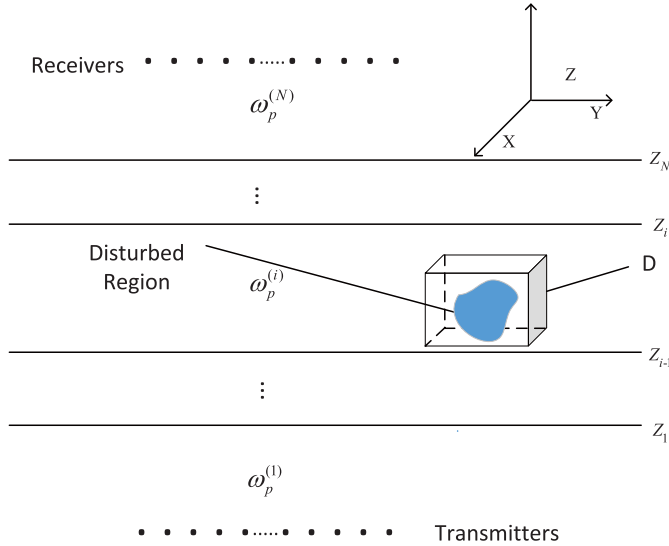
Fig. 1. Configuration for EM scattering by a disturbed plasma region in a planarly layered cold unmagnetized plasma medium.

parameter of a cold unmagnetized plasma medium and its value does not change with the angular frequency of EM waves. However, when the plasma is disturbed, the electron density in the disturbed region deviates from the background, and thus ω_p changes. Therefore, the disturbed region acts as the EM scatterer embedded in the background plasma.

Fig. 1 shows the configuration of the EM wave scattering by a disturbed plasma region with an arbitrary shape and embedded in a layered cold unmagnetized plasma medium, where the background has N layers with different plasma frequencies $\omega_p^{(n)}(n = 1, 2, \ldots, N)$, i.e., with different relative permittivity $\varepsilon_n(n = 1, 2, \ldots N)$ in each layer. The background plasma is homogeneous in the x- and y-directions but layered in the z-direction. The disturbed region completely contained in domain D can exist in any layer. In this letter, we assume it is located in layer i. The relative permittivity of the inhomogeneous disturbed region is ε. The transmitters are located in the bottom layer while the receivers are located in the top layer.

A. Forward Model

According to the electric field integral equations (EFIEs), the total field in the nth layer can be expressed as

$$\mathbf{E}_n(\mathbf{r}) = \mathbf{E}_n^{\text{inc}}(\mathbf{r}) - j\omega \left[\mathbf{A}^{\text{ni}}(\mathbf{r}) + \frac{1}{k_n^2}\nabla\nabla \cdot \mathbf{A}^{\text{ni}}(\mathbf{r}) \right]$$

$$\mathbf{A}^{\text{ni}}(\mathbf{r}) = j\omega\mu_n \int_D \mathbf{G}^{\text{ni}}(\mathbf{r}, \mathbf{r}')\chi_e(\mathbf{r}')\mathbf{D}_i(\mathbf{r}')d\mathbf{r}' \quad (3)$$

where $\mathbf{A}^{ni}(\mathbf{r})$ is the magnetic vector potential in the nth layer due to the induced current source $\mathbf{J}$ inside the disturbed region in the layer i, $\mathbf{D}_i$ is the electric flux density in the ith layer, $\chi_e = (\varepsilon - \varepsilon_i)/\varepsilon$ represents the electric contrast, $\mathbf{J} = \chi_e\mathbf{D}$, $\mathbf{G}^{\text{ni}}$ is the dyadic Green's function [19], [20], $\mathbf{E}_n$ denotes the total electric field in the nth layer, and $\mathbf{E}_n^{\text{inc}}$ denotes incident electric field in the absence of the disturbed region in the nth layer.

The grad-div operator $\nabla\nabla$ in (3) will bring about the singularity, so we choose the weak-form discretization [5], [21]

to eliminate it. We assume that the rectangular domain D with a dimension $R_x \times R_y \times R_z$ shown in Fig. 1 is discretized into uniform cubic cells. The grid cell sizes are Δx, Δy, and Δz in x-, y-, and z-directions the center of the cell is defined as

$$\mathbf{r}_{i,j,k} = \left[\left(i - \frac{1}{2}\right)\Delta x, \left(j - \frac{1}{2}\right)\Delta y, \left(k - \frac{1}{2}\right)\Delta z \right] \quad (4)$$

where $i \in [0, I]$, $j \in [0, J]$, $k \in [0, K]$, i, j, k are cell indices and L, M, N are cell numbers in x-, y-, and z-directions, respectively. The rooftop function [21] is used as the basis as well as testing functions in this letter. After discretization, the EFIE can be compactly written as a linear equation as [21]

$$\mathbf{e}^{\text{inc}} = [L]\mathbf{d} \quad (5)$$

where $[L]$ is a discrete linear operator, and $\mathbf{e}^{\text{inc}}$ and $\mathbf{d}$ denote the vectors of the incident electric field and the coefficient of unknown electric flux density expanded by basis functions, respectively. Solving the above equation directly is a very time-consuming process in the traditional method of moments, so we choose the BCGS-FFT method [9].

B. Inverse Model

In this letter, we select the VBIM to reconstruct the relative permittivity, and thus the plasma frequency of the disturbed region. The VBIM is elaborated in [17] and [18]. Due to the ill-posedness of the scattering problems, we need to construct a cost function by Tikhonov regularization [18]

$$F(\mathbf{x}) = \|\mathbf{f} - \mathbf{P}\mathbf{x}\|^2 + \gamma\|\mathbf{x}\|^2 \quad (6)$$

where the vector $\mathbf{f}$ represents difference between the measured scattered field in the observation domain and the computed scattered field by BCGS-FFT at the ith iteration, $\mathbf{P}$ is a 2-D matrix composed of Green's functions and total electric fields solved by the BCGS-FFT at the ith iteration, γ represents the regularization parameter, and $\mathbf{x}$ is a vector that contains electric contrast values in all the discretized cells. Our purpose is to obtain the stable solution, which is equivalent to finding the best $\mathbf{x}$ to minimize the cost function (6). This can be expressed by the following equation [18]:

$$(\mathbf{P}^\dagger\mathbf{P} + \gamma\mathbf{I})\mathbf{x} = \mathbf{P}^\dagger\mathbf{f} \quad (7)$$

where $\dagger$ denotes complex conjugate and transpose. The CG method [22] is chosen to efficiently solve this equation for obtaining the regularized solution minimizing the cost function.

Due to the dispersive property of the plasma, the electric contrast vector $\mathbf{x}$ in VBIM is a function of the operating frequency. Incident waves with different frequencies will lead to different retrieved relative permittivities, but the plasma frequency of the disturbed region remains unchanged. In this letter, multiple operating frequencies are used to reconstruct the relative permittivity and thus the plasma frequency of the same disturbed region.
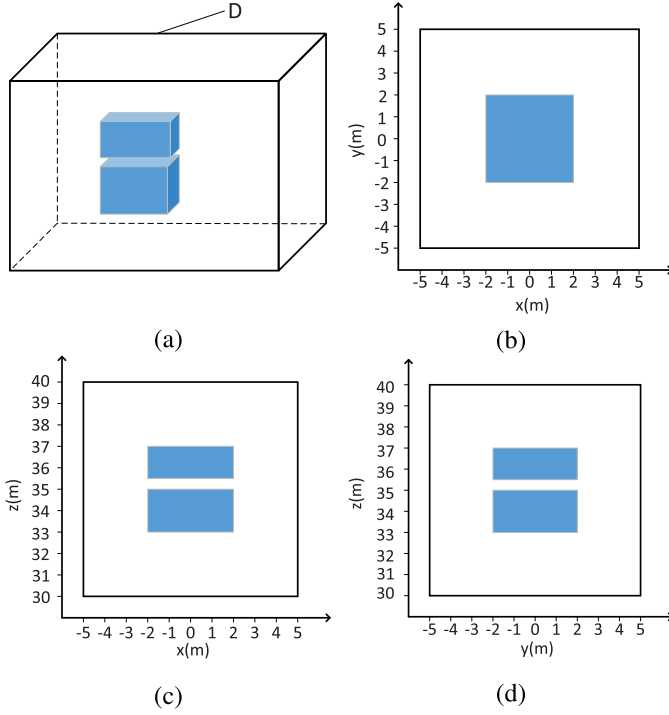
Fig. 2. Real geometry of the two-part disturbed region. (a) 3-D image. (b) Slice of the disturbed region in the xy plane. (c) Slice of the disturbed region in the xz plane. (d) Slice of the disturbed region in the yz plane.

Fig. 3. Comparison of the E_z^{sct} components of the scattered fields computed by the BCGS-FFT and simulated by Wavenology. (a) Real part of E_z^{sct} at 40 MHz. (b) Imaginary part of E_z^{sct} at 40 MHz. (c) Real part of E_z^{sct} at 50 MHz. (c) Imaginary part of E_z^{sct} at 50 MHz.

III. NUMERICAL RESULTS

In this section, we use two examples to illustrate the reconstruction of the relative permittivity and plasma frequency of the disturbed region in layered unmagnetized plasma media. The background medium has three layers with the boundary positions at $z_1 = 20$ m and $z_2 = 50$ m. The bottom layer is air, while the other two layers are cold unmagnetized plasma media with different plasma frequencies. The plasma frequencies of the middle layer and the top layer are 9.42×10^7 rad/s and 13.82×10^7 rad/s, respectively. The receivers are placed in the top layer, which vary from -4 to 5 m with an increment of 0.5 m in both the x- and y-directions while in the z-direction their coordinates are fixed values of 60 m. In order to enhance the accuracy of the retrieved permittivity contrast, we increase the antenna array radiating aperture and put the transmitters around the disturbed region. Their coordinates are (0 m, 0 m, 0 m), (2 m, 2 m, 27 m), (-2 m, 2 m, 27 m), (2 m, -2 m, 27 m), (-2 m, -2 m, 27 m), (6 m, 0 m, 35 m), (-6 m, 0 m, 35 m), (0 m, 6 m, 35 m), (0 m, -6 m, 35 m), (2 m, 2 m, 43 m), (-2 m, 2 m, 43 m), (2 m, -2 m, 43 m), (-2 m, -2 m, 43 m), and (0 m, 0 m, 43 m). Therefore, we have 14 transmitters and 361 receivers. The domain D, located in the middle layer, has a dimension $10 \times 10 \times 10$ m and is uniformly divided into $20 \times 20 \times 20$ cells. The center of the cell in the top-left corner locates at (-4.75 m, -4.75 m, 30.25 m). In our forward modeling and inversion process, we choose broadband signals instead of one single frequency. However, we just show the results of two different frequencies here due to the limitation of the contents of this letter.

In the first example, the disturbed region included in the domain D has two parts with different plasma frequencies.
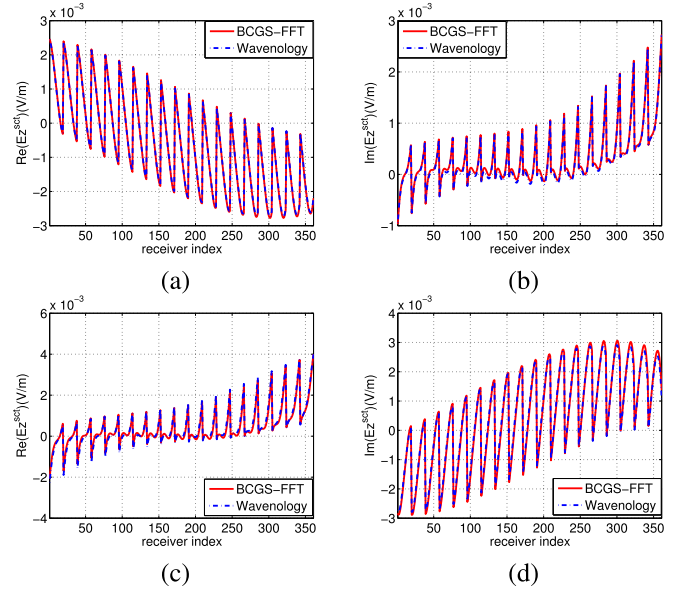
The geometries of both the parts are rectangular parallelepiped shapes that are depicted in Fig. 2. The lower part takes up the position from -2 m cell to 2 m in both the x- and y-directions and from 33 m cell to 35 m in the z-direction, while the top part takes up the position from the -2 to 2 m in both the x- and y-directions and from 35.5 to 37 m in the z-direction. The plasma frequency of the lower part is $\omega_{p1} = 12.56 \times 10^7$ rad/s while that of the upper part is $\omega_{p2} = 6.28 \times 10^7$ rad/s. We choose the operating frequencies as 40 and 50 MHz. Thus, the relative permittivities of the background from the bottom layer to the top layer are 1, 0.86, 0.70 at 40 MHz and 1, 0.91, 0.81 at 50 MHz, respectively. The relative permittivities of the lower and upper parts of the disturbed region are 0.75 and 0.938 at 40 MHz and 0.84 and 0.96 at 50 MHz, respectively. Before inversion, the scattered field needed for inversion is calculated by forward BCGS-FFT method. So, we first validate the effectiveness of the BCGS-FFT method.

In the second example, the disturbed region is one single cube included in the domain D, which takes up the position from the -2 m to 2 m in both the x- and y-directions and from 33 to 37 m in the z-direction. The geometry is simpler than that of the last one and thus we do not plot its figure here. Its plasma frequency is 12.56×10^7 rad/s. Two operating frequencies of 35 and 45 MHz are used. Thus, the relative permittivities of the background from the bottom layer to the top layer are 1, 0.82, 0.61 at 35 MHz and 1, 0.89, 0.76 at 45 MHz, respectively. The relative permittivity of the disturbed region is 0.67 at 35 MHz and 0.80 at 45 MHz.

A. Forward Validation

Fig. 3 shows the compared results of the scattered fields computed by BCGS-FFT and simulated by the commercial software Wavenology. Although the compared results of all components of the scattered fields have excellent agreements,
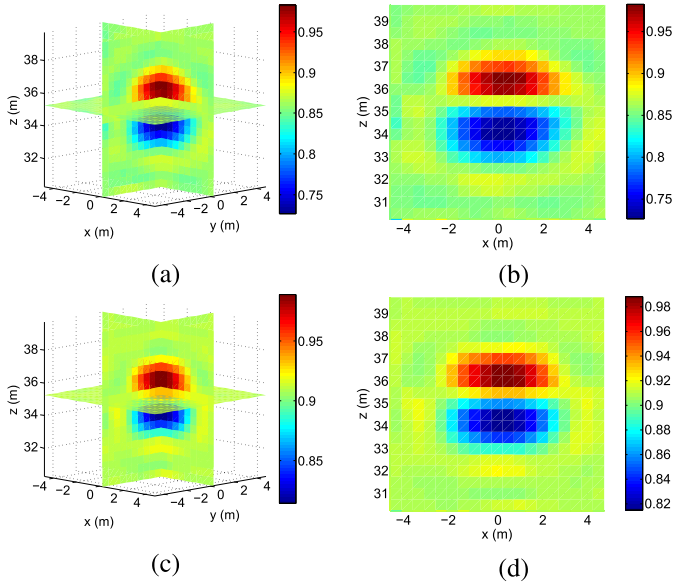
Fig. 4. Reconstructed relative permittivity of the disturbed region. (a) 3-D slices at 40 MHz. (b) Slice along the center of the disturbed region in the xz plane at 40 MHz. (c) 3-D slice at 50 MHz. (d) Slice along the center of the disturbed region in the xz plane at 50 MHz.

we only show the E_z component here due to the content limitation of this letter. We define the relative error between BCGS-FFT computations and Wavenology simulations as

$$E_{\mathrm{rr}} = \frac{\left\| \mathbf{E}_{\mathrm{sim}}^{\mathrm{sca}} - \mathbf{E}_{\mathrm{com}}^{\mathrm{sca}} \right\|}{\left\| \mathbf{E}_{\mathrm{sim}}^{\mathrm{sca}} \right\|} \tag{8}$$

where $\mathbf{E}_{\mathrm{sim}}^{\mathrm{sca}}$ represents the simulated scattered field by Wavenology, and $\mathbf{E}_{\mathrm{com}}^{\mathrm{sca}}$ represents the computed scattered field by BCGS-FFT.

From Fig. 3, it can be observed that the two curves match nicely with each other for both the real and imaginary parts at both the frequencies. The relative errors are 4.5% at 40 MHz and 2.8% at 50 MHz.

B. Three-Dimensional Reconstruction of the Relative Permittivity and Plasma Frequency of the Disturbed Region

In order to quantify the error of reconstruction, we define the relative residual error (RRE) as

$$\mathrm{RRE} = \frac{\left\| \mathbf{E}_{\mathrm{meas}}^{\mathrm{sca}} - \mathbf{E}_{(i)}^{\mathrm{sca}} \right\|}{\left\| \mathbf{E}_{\mathrm{meas}}^{\mathrm{sca}} \right\|} \tag{9}$$

where $\mathbf{E}_{\mathrm{meas}}^{\mathrm{sca}}$ represents the measured scattered field and $\mathbf{E}_{(i)}^{\mathrm{sca}}$ represents the scattered field computed by VBIM at the ith iteration step. During the iteration, when the RRE is less than the prescribed error threshold 10^{-6} we set, the computing process [18] will stop immediately.

In the first example, from the description above, we know that the permittivity contrast of the upper part with respect to its background is positive, while that of the lower part is negative. We apply the VBIM algorithm described in Section II to the retrieval of the disturbed plasma region. It takes 11 iterations to obtain the relative permittivity and plasma frequency. Figs. 4 and 5 show the reconstructed results.
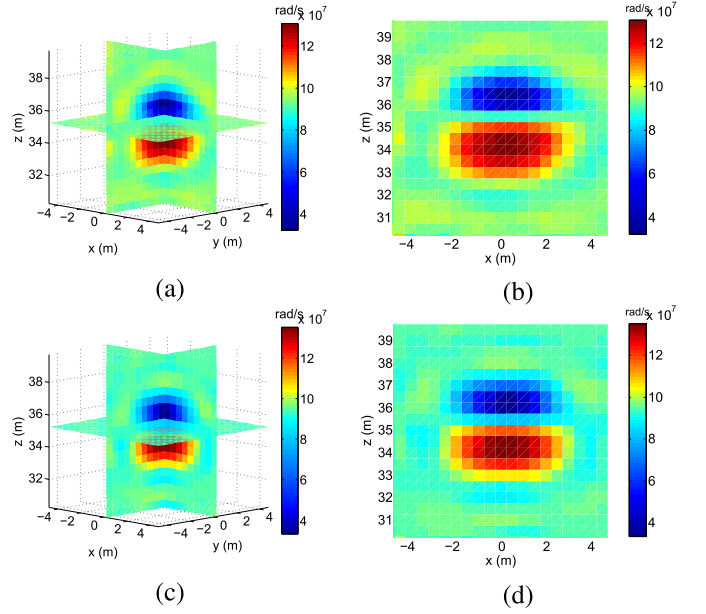

Fig. 5. Reconstructed plasma frequency of the disturbed region. (a) 3-D slice at 40 MHz. (b) Slice along the center of the disturbed region in the xz plane at 40 MHz. (c) 3-D slice at 50 MHz. (d) Slice along the center of the disturbed region in the xz plane at 50 MHz.
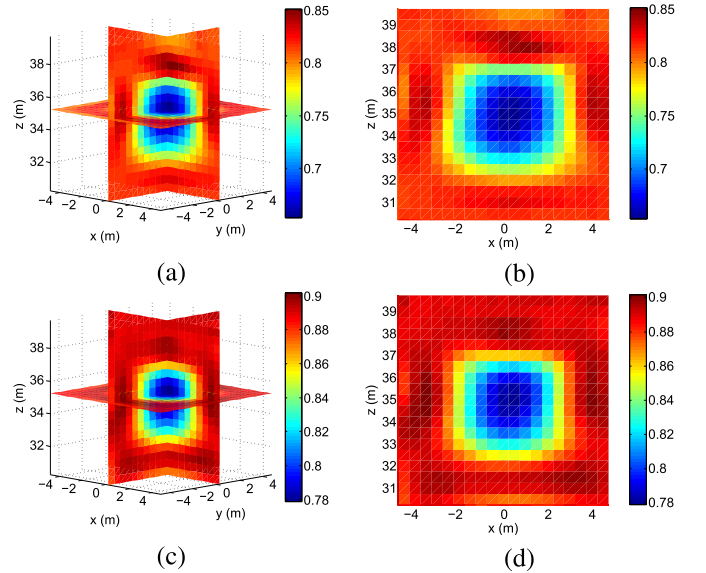

Fig. 6. Reconstructed relative permittivity of the disturbed region. (a) Three-dimensional slice at 35 MHz. (b) Slice along the center of the disturbed region in the xz plane at 35 MHz. (c) Three-dimensional slice at 45 MHz. (d) Slice along the center of the disturbed region in the xz plane at 45 MHz.

We observe that the reconstructed relative permittivity and the plasma frequency of the disturbed region are close to the true values. Besides, the reconstructed plasma frequency of the two disturbed regions remains unchanged at these two operating frequencies although the reconstruct permittivities are different. The locations and shapes of the two parts of the disturbed region can be clearly identified from the 2-D slices.

In the second example, it is obvious that the permittivity contrast of the disturbed region with respect to its background is negative. It takes 11 iterations to obtain the relative permittivity and plasma frequency. Fig. 6 shows the reconstructed
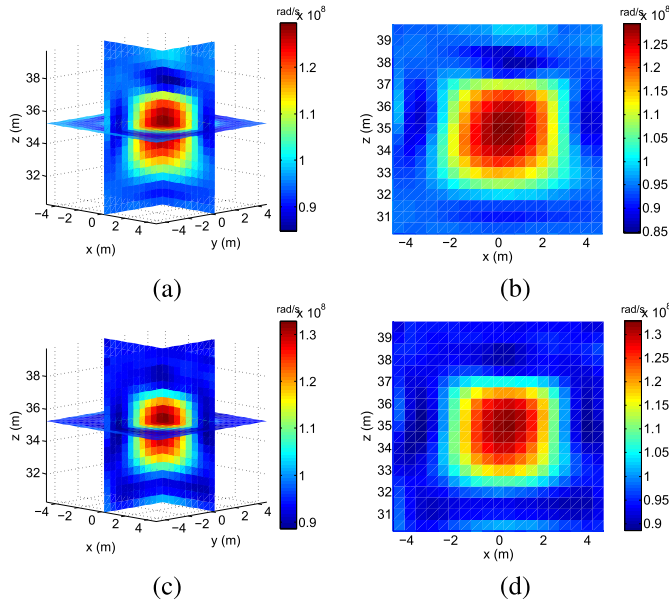
Fig. 7. Reconstructed plasma frequency of the disturbed region. (a) Three-dimensional slice at 35 MHz. (b) Slice along the center of the disturbed region in the xz plane at 35 MHz. (c) Three-dimensional slice at 45 MHz. (d) Slice along the center of the disturbed region in the xz plane at 45 MHz.

relative permittivity and Fig. 7 shows the reconstructed plasma frequency of the disturbed region at two operating frequencies based on the VBIM algorithm. We noticed that the relative permittivity and the plasma frequency of the disturbed region are well reconstructed both at 35 and 45 MHz. The reconstructed results are extremely close to the true values. Besides, the retrieved plasma frequency of the disturbed region remains almost unchanged even if the operating frequency changes. It is also clearly found from the 2-D slices of the figures that the locations and shapes of the disturbed region are well reconstructed.

IV. CONCLUSION

In this letter, forward scattering and inverse scattering of a disturbed region in a layered cold unmagnetized plasma medium are discussed. This is the first time that the 3-D cold unmagnetized plasma medium inverse scattering problem is investigated. Thanks to the effectiveness of the BCGS-FFT-VBIM, it is possible to reconstruct accurately the relative permittivity and thus the plasma frequency of the disturbed region. In our numerical experiments, the reconstructed relative permittivity and plasma frequencies are nearly equal to the true values. Moreover, it turns out that the reconstructed plasma frequency of the disturbed region does not change when the operating frequency varies. This fully reflects the dispersive property of the cold unmagnetized plasma medium. To date, the inversion is performed based on a single frequency, although we use multiple frequencies to validate the results. The future work will focus on the multifrequency joint inversion. The electron density instead of the plasma frequency will be retrieved directly. The successful reconstruction of the disturbed region in cold unmagnetized plasma media will make a valuable contribution to the material characterization target identification.

REFERENCES

[1] F. Li, Q. H. Liu, and L.-P. Song, "Three-dimensional reconstruction of objects buried in layered media using Born and distorted Born iterative methods," *IEEE Geosci. Remote Sens. Lett.*, vol. 1, no. 2, pp. 107–111, Apr. 2004.

[2] T. J. Cui and W. C. Chew, "Novel diffraction tomographic algorithm for imaging two-dimensional targets buried under a lossy earth," *IEEE Trans. Geosci. Remote Sens.*, vol. 38, no. 4, pp. 2033–2041, Jul. 2001.

[3] Y. Yu, J. Niu, and J. J. Simpson, "A 3-D global earth-ionosphere FDTD model including an anisotropic magnetized plasma ionosphere," *IEEE Trans. Antennas Propag.*, vol. 60, no. 7, pp. 3246–3256, Jul. 2012.

[4] S. Liu, J. Mo, and N. Yuan, "Research on the relation between unmagnetized plasma density and the stealth of target," *J. Radio Sci.*, vol. 18, no. 1, pp. 57–61, Feb. 2003.

[5] Z. Q. Zhang and Q. H. Liu, "Three-dimensional weak-form conjugate- and biconjugate-gradient FFT methods for volume integral equations," *Microw. Opt. Technol. Lett.*, vol. 29, no. 5, pp. 350–356, Jun. 2001.

[6] T. F. Eibert, "A diagonalized multilevel fast multipole method with spherical harmonics expansion of the k-space integrals," *IEEE Trans. Antennas Propag.*, vol. 53, no. 2, pp. 814–817, Feb. 2005.

[7] W.-B. Ewe, E.-P. Li, H.-S. Chu, and L.-W. Li, "AIM analysis of electromagnetic scattering by arbitrarily shaped magnetodielectric object," *IEEE Trans. Antennas Propag.*, vol. 55, no. 7, pp. 2073–2079, Jul. 2007.

[8] X. Xu, Q. H. Liu, and Z. W. Zhang, "The stabilized biconjugate gradient fast Fourier transform method for electromagnetic scattering," *Antennas Propag. Soc. Int. Symp.*, vol. 2. Jun. 2002, pp. 614–617.

[9] X. Millard and Q. H. Liu, "A fast volume integral equation solver for electromagnetic scattering from large inhomogeneous objects in planarly layered media," *IEEE Trans. Antennas Propag.*, vol. 51, no. 9, pp. 2393–2401, Sep. 2003.

[10] Z. Q. Zhang and Q. H. Liu, "Applications of the BCGS-FFT method to 3-D induction well logging problems," *IEEE Trans. Geosci. Remote Sens.*, vol. 41, no. 5, pp. 998–1004, May 2003.

[11] X. Millard and Q. H. Liu, "Simulation of near-surface detection of objects in layered media by the BCGS-FFT method," *IEEE Trans. Geosci. Remote Sens.*, vol. 42, no. 2, pp. 327–334, Feb. 2004.

[12] C. Yu, M. Yuan, and Q. H. Liu, "Reconstruction of 3D objects from multi-frequency experimental data with a fast DBIM-BCGS method," *IEEE Trans. Med. Imag.*, vol. 9, no. 2, pp. 218–225, Jan. 1990.

[13] A. Abubakar, P. M. V. D. Berg, and J. J. Mallorqui, "Imaging of biomedical data using a multiplicative regularized contrast source inversion method," *IEEE Trans. Microw. Theory Techn.*, vol. 50, no. 7, pp. 1761–1771, Jul. 2002.

[14] X. Chen, D. Liang, and K. Huang, "Microwave imaging 3-D buried objects using parallel genetic algorithm combined with FDTD technique," *J. Electromagn. Waves Appl.*, vol. 20, no. 13, pp. 1761–1774, Sep. 2012.

[15] Y. Zhong and X. Chen, "MUSIC imaging and electromagnetic inverse scattering of multiple-scattering small anisotropic spheres," *IEEE Trans. Antennas Propag.*, vol. 55, no. 12, pp. 3542–3549, Dec. 2007.

[16] J. H. Shen, Y. Zhong, X. Chen, and L. Ran, "Inverse scattering problems of reconstructing perfectly electric conductors with TE illumination," *IEEE Trans. Antennas Propag.*, vol. 61, no. 9, pp. 4713–4721, Sep. 2013.

[17] Z. Nie, F. Yang, Y. Zhao, and Y. Zhang, "Variational Born iteration method and its applications to hybrid inversion," *IEEE Trans. Geosci. Remote Sens.*, vol. 38, no. 4, pp. 1709–1715, Jul. 2000.

[18] W. Zhang and Q. H. Liu, "Three-dimensional scattering and inverse scattering from objects with simultaneous permittivity and permeability contrasts," *IEEE Trans. Geosci. Remote Sens.*, vol. 53, no. 4, pp. 429–439, Jan. 2015.

[19] K. A. Michalski and J. R. Mosig, "Multilayered media Green's functions in integral equation formulations," *IEEE Trans. Antennas Propag.*, vol. 45, no. 3, pp. 508–519, Mar. 1997.

[20] J. K. Lee and J. A. Kong, "Dyadic Green's functions for layered anisotropic medium," *Electromagnetics*, vol. 3, pp. 111–130, Sep. 1983.

[21] P. Zwamborn and P. M. van den Berg, "The three dimensional weak form of the conjugate gradient FFT method for solving scattering problems," *IEEE Trans. Microw. Theory Technol.*, vol. 40, no. 9, pp. 350–356, Jun. 1992.

[22] T. J. Peters and J. L. Volakis, "Application of a conjugate gradient FFT method to scattering from thin planar material plates," *IEEE Trans. Antennas Propag.*, vol. 36, no. 4, pp. 518–526, Apr. 1988.